Physica B 737 (2026) 418742

Contents lists available at ScienceDirect

Physica B: Condensed Matter

journal homepage: www.elsevier.com/locate/physb

Ettingshausen effect in GaAs/AlGaAs superlattices

D. Sekyi-Arthur [a,c,*], S.Y. Mensah [b], K.A. Dompreh [b]

[a] Department of Physics, College of Basic and Applied Sciences, University of Ghana, PMB, Accra, Ghana
[b] Department of Physics, College of Agriculture and Natural Sciences, University of Cape Coast, PMB, Cape Coast, Ghana
[c] Centre for Quantum Transport in Advanced Materials, University of Ghana, PMB, Accra, Ghana

ARTICLE INFO

Keywords:
Ettingshausen effect
Superlattices
Thermomagnetic transport
Boltzmann transport equation
Miniband structure
Thermal conductivity

ABSTRACT

We present a theoretical investigation of the Ettingshausen effect — the generation of a transverse temperature gradient under the action of an applied electric current — in GaAs/AlGaAs superlattices subjected to combined dc–ac electric fields and an external magnetic field. Using the Boltzmann transport equation (BTE) in the constant relaxation-time approximation, explicit expressions for the longitudinal and transverse Ettingshausen coefficients are derived in terms of the miniband width, chemical potential, magnetic field strength, and thermal conductivity. Analytical asymptotics reveal that at high temperatures, both coefficients saturate to finite plateaus, while at low temperatures, they exhibit strong non-monotonic behaviour and possible sign reversals depending on the superlattice parameter values. Numerical analysis demonstrates that increasing the miniband width enhances the low-temperature response, higher chemical potentials suppress and may invert the effect, and stronger magnetic fields or larger thermal conductivities reduce the net magnitude. These results show that the Ettingshausen effect in superlattices is highly tunable through band structure and external controls, suggesting opportunities for thermomagnetic cooling, field sensing, and nanoscale energy conversion applications.

1. Introduction

The interplay between electric, thermal, and magnetic transport in solids gives rise to a rich class of thermomagnetic phenomena. Among these, the Ettingshausen effect — the generation of a transverse temperature gradient under the action of an applied electric current in a magnetic field — provides a powerful probe of charge carrier dynamics, scattering processes, and band structure [1,2]. It is intricately linked to the Nernst effect and belongs to a classification of galvanomagnetic and thermoelectric phenomena that have been studied since the early 20th century [3,4] popularly known as the *Nernst–Ettingshausen effect*. The Ettingshausen effect, while well-documented in bulk metals and semiconductors, has recently attracted renewed attention due to its prospective uses in enhanced cooling technologies, thermomagnetic sensors, and energy conversion devices [5,6].

The emergence of artificially engineered materials, particularly semiconductor superlattices (SSLs), has created new opportunities for investigating thermomagnetic transport in lower dimensions. A superlattice, initially conceived and experimentally shown by Esaki and Tsu [7], comprises alternating thin layers of semiconductors that create a periodic potential, resulting in the division of the electronic band structure into minibands. The miniband transport regime facilitates distinct regulation of charge carrier dynamics, miniband width, and scattering processes, characteristics which are absent in bulk systems [8,9]. Consequently, SLs have emerged as attractive platforms for optimizing thermoelectric and thermomagnetic effects beyond bulk limitations [10–12].

Several theoretical and experimental efforts have examined thermoelectric and related effects in SLs. For instance, Mensah and coworkers [13,14] analysed the thermomagnetic effect under crossed electric and magnetic fields, demonstrating the sensitivity of transport coefficients to miniband parameters and external conditions. Research has shown recently how quantum confinement, nonlinear field effects, and strong electron–phonon coupling modifies the thermomagnetic responses in nanoscale systems [15–17].

However, there has been a significant rise of interest in nanoscale and nanostructured thermoelectrics, where better control over scattering and density of states permits high-efficiency heat management [18,19]. Nanostructured SLs and quantum wells have been constructed to suppress phonon transport while enhancing or improving carrier conduction, which results in significant improvements in thermoelectric figures of merit [20,21]. Such results show that the Ettingshausen effect, which for long was perceived to be a classical transport metric, can be greatly modified and potentially optimized in nanostructured systems.

* Corresponding author at: Department of Physics, College of Agriculture and Natural Sciences, University of Cape Coast, PMB, Cape Coast, Ghana.
E-mail addresses: dsekyi-arthur@ug.edu.gh, rasdean3@gmail.com (D. Sekyi-Arthur).

https://doi.org/10.1016/j.physb.2026.418742
Received 22 March 2026; Received in revised form 20 April 2026; Accepted 30 April 2026
Available online 5 May 2026

Despite these developments, full theoretical treatments of the Ettingshausen effect in SLs, particularly under mixed dc and ac electric fields, are still limited. The existence of both static and time-varying fields adds complexity via field-induced miniband modulation, Bessel-function-dependent dressing factors, and cyclotron frequency effects. A comprehensive investigation of the impact of factors like miniband width, chemical potential, magnetic field intensity, and thermal conductivity on the Ettingshausen coefficients is essential for both basic understanding and practical use.

Unlike a purely static dc bias, the ac component periodically modulates the carrier quasi-momentum and miniband velocity, thereby enabling photon-assisted transport and dynamic renormalization of the effective drift response. Within the semiclassical picture, the resulting cycle-averaged transport contains Bessel-type factors $J_n(e\mathcal{E}_{ac}d/\hbar\omega)$, allowing suppression, enhancement, or sign control of the Ettingshausen response through the field amplitude and frequency. This provides a functional advantage of dynamic tunability not accessible under dc excitation alone.

In this manuscript, we present a theoretical study of the Ettingshausen effect in SLs using the BTE under constant relaxation time. We derive explicit analytical expressions for both transverse and longitudinal Ettingshausen coefficients and analyse their dependence on temperature, miniband width, chemical potential, magnetic field, and thermal conductivity. The results reveal tunable and non-monotonic temperature behaviour, including high-temperature plateaus, low-temperature amplification, and possible sign reversals. These findings not only provide insight into the physics of thermomagnetic transport in low-dimensional systems but also suggest potential applications in nanoscale cooling, magnetic field sensing, and thermomagnetic energy conversion.

2. Theoretical model and system setup

We consider charge carrier transport in a SSL subjected to a static magnetic field and an external electromagnetic wave. The system is described within a semiclassical framework, where the carrier dynamics are governed by the BTE and quantum effects enter only through the miniband energy dispersion relation. In contrast to approaches based on Landau-level quantization, the present treatment assumes that the magnetic field is sufficiently weak or the temperature sufficiently high such that Landau quantization is suppressed and the carrier motion remains quasi-continuous in momentum space.

We clarify that the present work considers a SL and does not include a carbon nanotube as a physical component. The apparent similarity arises because the tight-binding miniband dispersion used in this work is mathematically analogous to models employed in quasi-one-dimensional systems such as carbon nanotubes (see Fig. 1).

We consider a SL structure in which electron motion along the growth direction (x-axis) is governed by a single miniband described within the tight-binding approximation. The transverse directions (y, z) retain free-electron parabolic dispersion. Transport is treated within the semiclassical Boltzmann transport framework under the constant relaxation-time approximation, assuming that electrons remain confined to the lowest miniband. No explicit external leads are included; the model describes intrinsic bulk transport within the superlattice.

The system is subjected to:

- Magnetic field $\vec{\mathcal{H}} \parallel z$
- Electric current density $\vec{J}_x$
- Transverse temperature gradient $\nabla_y T$
- AC electric field orientation

The electromagnetic fields are introduced through the scalar and vector potentials, $\phi(\mathbf{r},t)$ and $\vec{\mathcal{A}}(\mathbf{r},t)$, defined by

$$\vec{\mathcal{E}}(\vec{r},t) = -\nabla\phi(\vec{r},t) - \frac{1}{c}\frac{\partial\vec{\mathcal{A}}(\vec{r},t)}{\partial t}, \qquad \vec{\mathcal{H}} = \nabla\times\vec{\mathcal{A}}(\vec{r},t). \tag{1}$$

For a uniform static magnetic field $\vec{\mathcal{H}} = \mathcal{H}\hat{z}$ and a linearly polarized electromagnetic wave propagating along the superlattice axis, a convenient choice of gauge is the Landau gauge given as

$$\vec{\mathcal{A}}(\vec{r},t) = \left(0,\ \mathcal{H}x,\ \mathcal{A}_{\rm ac}\cos\omega t\right), \tag{2}$$

with $\phi(\vec{r},t) = 0$. This gauge preserves translational invariance along the y- and z-directions and allows the time-dependent field to be incorporated naturally through the vector potential. It is important to note that the physical observables derived below are gauge invariant; the explicit gauge choice serves only to simplify the analytical treatment.

In the absence of Landau quantization, the carrier motion is described by the semiclassical equations of motion

$$\dot{\vec{r}} = \frac{1}{\hbar}\nabla_{\vec{k}}\vartheta(\vec{k}), \qquad \hbar\dot{\vec{k}} = -e\left[\vec{\mathcal{E}}(t) + \frac{1}{c}\dot{\vec{r}}\times\vec{\mathcal{H}}\right], \tag{3}$$

where $\vartheta(\vec{k})$ is the miniband energy dispersion of the superlattice.

The energy of the carriers in the lowest miniband using the tight-binding approach for the semiconductor superlattice is given as

$$\vartheta(\vec{p}) = \frac{p_y^2 + p_z^2}{2m^*} + \Delta[1 - \cos(\frac{p_x d}{\hbar})], \tag{4}$$

where m^* is the effective mass in the plane of the layers, Δ is the miniband width, and d is the superlattice period. The carrier velocities defined as $\vec{v} = \nabla_{\vec{p}}\vartheta(\vec{p})$, along the crystallographic directions are given as:

$$v_x = \frac{\Delta d}{\hbar}\sin\left(\frac{p_x d}{\hbar}\right), \quad v_y = \frac{p_y}{m^*}, \quad v_z = \frac{p_z}{m^*}. \tag{5}$$

Since the magnetic field enters only through the Lorentz force in Eq. (3), the transverse dynamics are modified continuously rather than discretized into Landau levels. For GaAs/AlGaAs superlattices, the weak-field regime corresponds to $\hbar\omega_c \ll kT, \Delta, \Gamma$. Using $m^* = 0.067m_e$, this condition is typically satisfied for $\mathcal{H} \lesssim 0.5$–$2\,\mathrm{T}$, depending on temperature and scattering broadening, and $\omega_c\tau \lesssim 1$, where $\omega_c = e\mathcal{H}/(m^*c)$ is the cyclotron frequency and τ is the momentum relaxation time.

The electromagnetic fields enter the BTE exclusively through the gauge-invariant combination of $\vec{\mathcal{E}}$ and $\vec{\mathcal{H}}$ appearing in Eq. (3) as

$$\frac{\partial F(\vec{r},\vec{p},t)}{\partial t} + v(\vec{p}).\nabla_r F(\vec{r},\vec{p},t) + e\left\{\vec{\mathcal{E}}(t) + \vec{\mathcal{E}}_0 + \frac{1}{c}[\vec{v}(p)\times\vec{\mathcal{H}}]\right\}\nabla_p F(\vec{r},\vec{p},t) = -\frac{F(\vec{r},\vec{p},t) - F_0(\vec{p})}{\tau}. \tag{6}$$

As a result, the transport coefficients derived from the solution of BTE depend only on the physical fields and not on the specific choice of gauge.

The semiclassical BTE in the presence of an electric field $\vec{\mathcal{E}}$, magnetic field $\vec{\mathcal{H}}$, and temperature gradient under steady-state and spatially uniform conditions is obtained as,

$$\vec{v}\cdot\nabla_r F_0(\vec{p}) = \vec{v}\cdot\left(\frac{\partial F_0(\vec{p})}{\partial T}\nabla T\right). \tag{7}$$

Since the equilibrium distribution function depends on position only through the local temperature field, i.e. $F_0 = F_0(\vartheta(\vec{p}), T(\mathbf{r}))$, its spatial derivative follows directly from the chain rule as

$$\nabla_{\mathbf{r}} F_0 = \frac{\partial F_0}{\partial T}\nabla T,$$

where the carrier energy $\vartheta(\vec{p})$ is spatially uniform. The first-order correction $F_1(\vec{p})$ then satisfies

$$F_1(\vec{p}) = -\tau\left[\vec{v}\cdot\left(\frac{\partial F_0(\vec{p})}{\partial T}\nabla T\right) + e\left(\vec{\mathcal{E}} + \frac{\vec{v}\times\vec{\mathcal{H}}}{c}\right)\cdot\nabla_p F_0(\vec{p})\right], \tag{8}$$

whose tensorial solution may be written as [8,22]

$$F_1(\vec{p}) = -\tau_{\rm eff}\,(\vartheta - \varrho)\frac{\partial F_0(\vec{p})}{\partial\vartheta}\left(A_{ik}v_k\right)\nabla_i T. \tag{9}$$

In this context, $F_0(\vec{p})$ represents the equilibrium distribution function, $\vec{v}(\vec{p})$ denotes the carrier velocity, $\mathcal{E}$ denotes a weak constant applied

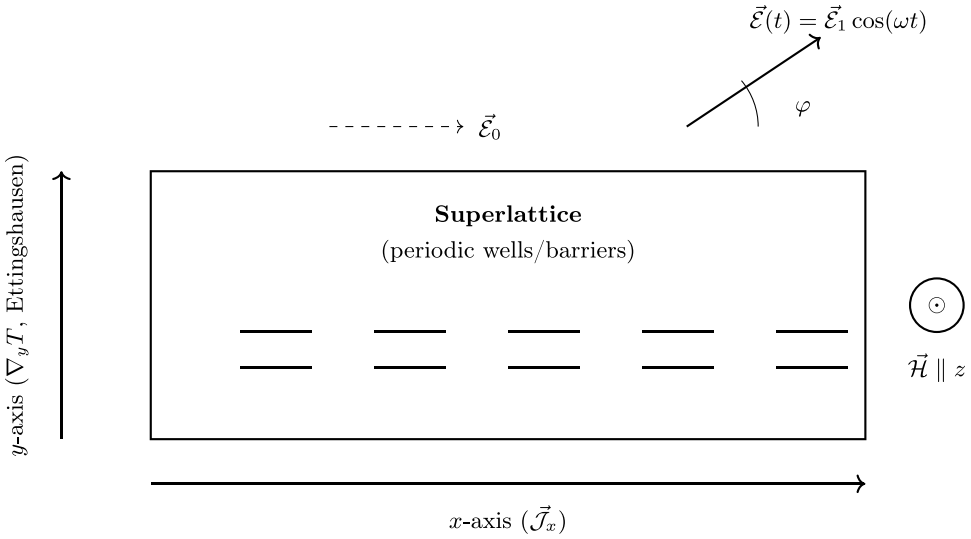

Fig. 1. Schematic diagram of the semiconductor superlattice system illustrating the Ettingshausen effect. The superlattice is oriented along the x-axis, along which an electric current density $\vec{J}_x$ flows under the influence of an applied electric field. A magnetic field $\vec{\mathcal{H}}$ is applied perpendicular to the plane (along the z-axis), resulting in a transverse temperature gradient $\nabla_y T$ along the y-axis. An AC electric field $\vec{\mathcal{E}}(t) = \vec{\mathcal{E}}_1 \cos(\omega t)$ is applied in the plane at an angle φ to the superlattice axis.

field, $\vec{r}$ denotes the carrier position, $\vec{p}$ represents the electrodynamical momentum, τ is the relaxation time, and e denotes the electronic charge.

The constant relaxation-time approximation makes the derivations less rigorous and captures the leading transport trends but neglects the explicit energy dependence of scattering. If $\tau = \tau(\vartheta)$, the quantitative locations and amplitudes of low-temperature extrema may be modified. Nevertheless, the predicted sign reversals primarily originate from band-structure asymmetry and magnetic deflection, and are therefore expected to remain qualitatively valid.

The collision integral is estimated with the $1/\tau$ approximation and then assumed to be constant. The iterative technique with the initial condition $F(\vec{p}, -\infty) = F_0(\vec{p})$ is used for the linear approximation of $\mathcal{E}_0$, ∇T, $\mathcal{H}$, and $\nabla\varrho$. The resolution of the BTE, the carrier and thermal current densities are obtained via periodic averaging by following Refs. [12–14,23–26].

Combining Eqs. (7)–(9) and following Mensah and co-workers [13, 14], the full resolution of the BTE via periodic averaging is represented as

$$
\begin{aligned}
F(\vec{p}) &= \frac{\omega}{2\pi\tau}\int_0^{2\pi/\omega} dt \int_{-\infty}^{t} dt_1 \int_{-\infty}^{t_1} dt_2 \exp\left(\frac{t-t_2}{\tau}\right) \\
&\times \sum_p \left((e\vartheta_k - \nabla_k\varrho) + [\vartheta(\vec{p}) - \varrho]\frac{\nabla_k T}{T}\right) \frac{\partial F_o(\vec{p})}{\partial p_k} \\
&+ \frac{e\omega}{2\pi\tau c}\int_0^{2\pi/\omega} dt \int_{-\infty}^{t} dt_1 \int_{-\infty}^{t_1} dt_2 \int_{-\infty}^{t_2} dt_3 \exp\left(\frac{t-t_3}{\tau}\right) \\
&\times \sum_p \left((e\vartheta_k - \nabla_k\varrho) + [\vartheta(\vec{p}) - \varrho]\frac{\nabla_k T}{T}\right) \\
&\times \left[v_i\left(\vec{p} + e\int_{t_2}^{t} \vec{\mathcal{E}}(t')dt'\right) \times \vec{\mathcal{H}}\right] \frac{\partial^2 F_o(\vec{p})}{\partial p_k \partial p_j}.
\end{aligned} \tag{10}
$$

The carrier current density is defined as

$$
\vec{\mathcal{J}} = e\sum_p \vec{v}(\vec{p}) F(\vec{r}, \vec{p}, t) \qquad \vec{\mathcal{Q}} = \sum_p [\vartheta(\vec{p}) - \varrho]\vec{v}(\vec{p}) F(\vec{r}, \vec{p}, t) \tag{11}
$$

Substituting Eq. (10) into Eq. (11) we obtain

$$
\begin{aligned}
J_i &= \frac{e\omega}{2\pi\tau}\int_0^{2\pi/\omega} dt \int_{-\infty}^{t} dt_1 \int_{-\infty}^{t_1} dt_2 \exp\left(\frac{t-t_2}{\tau}\right) \\
&\times \sum_p \left((e\vartheta_k - \nabla_k\varrho) + [\vartheta(\vec{p}) - \varrho]\frac{\nabla_k T}{T}\right) v_i\left(\vec{p} + e\int_{t_2}^{t} \vec{\mathcal{E}}(t')dt'\right) \frac{\partial F_o(\vec{p})}{\partial p_k} \\
&+ \frac{e^2\omega}{2\pi\tau c}\int_0^{2\pi/\omega} dt \int_{-\infty}^{t} dt_1 \int_{-\infty}^{t_1} dt_2 \int_{-\infty}^{t_2} dt_3 \exp\left(\frac{t-t_3}{\tau}\right) \\
&\times \sum_p \left((e\vartheta_k - \nabla_k\varrho) + [\vartheta(\vec{p}) - \varrho]\frac{\nabla_k T}{T}\right) v_i\left(p + e\int_{t_2}^{t} \vec{\mathcal{E}}(t')dt'\right) \\
&\times \left[v_i\left(\vec{p} + e\int_{t_2}^{t} \vec{\mathcal{E}}(t')dt'\right), \vec{\mathcal{H}}\right] \frac{\partial^2 F_o(\vec{p})}{\partial p_k \partial p_j}
\end{aligned} \tag{12}
$$

Analogously, the carrier thermal-current density is expressed as

$$
\begin{aligned}
Q_i &= \frac{e\omega}{2\pi\tau}\int_0^{2\pi/\omega} dt \int_{-\infty}^{t} dt_1 \int_{-\infty}^{t_1} dt_2 \exp\left(\frac{t-t_2}{\tau}\right) \\
&\times \sum_p [\vartheta(\vec{p}) - \varrho]\left((e\vartheta_k - \nabla_k\varrho) + [\vartheta(\vec{p}) - \varrho]\frac{\nabla_k T}{T}\right) v_i\left(\vec{p} + e\int_{t_2}^{t} \vec{\mathcal{E}}(t')dt'\right) \frac{\partial F_0(\vec{p})}{\partial p_k} \\
&+ \frac{e^2\omega}{2\pi\tau c}\int_0^{2\pi/\omega} dt \int_{-\infty}^{t} dt_1 \int_{-\infty}^{t_1} dt_2 \int_{-\infty}^{t_2} dt_3 \exp\left(\frac{t-t_3}{\tau}\right) \\
&\times \sum_p [\vartheta(\vec{p}) - \varrho]\left((e\vartheta_k - \nabla_k\varrho) + [\vartheta(\vec{p}) - \varrho]\frac{\nabla_k T}{T}\right) v_i\left(\vec{p} + e\int_{t_2}^{t} \vec{\mathcal{E}}(t')dt'\right) \\
&\times \left[v_i\left(\vec{p} + e\int_{t_2}^{t} \vec{\mathcal{E}}(t')dt'\right), \vec{\mathcal{H}}\right] \frac{\partial^2 F_o(\vec{p})}{\partial p_k \partial p_j}
\end{aligned} \tag{13}
$$

The outcomes delineated by the linear response relation are as follows:

$$
J_i = \sigma_{ik}\mathcal{E}_k^* - \beta_{ik}\nabla_k T, \qquad Q_i = \gamma_{ik}\mathcal{E}_k^* - \chi_{ik}\nabla_k T, \tag{14}
$$

where i represents the direction of current and k represents the direction of the driving force. Einstein summation over repeated indices is implied.

We substitute Eq. (4) into Eq. (12) and Eq. (13) and solve the resultant equations for J_i and Q_i in the context of a non-degenerate electron gas, where $\mathcal{E}_k^*$ is the effective electric field, and is defined as:

$$
\mathcal{E}_k^* = \mathcal{E}_{0k} + \frac{1}{e}\frac{\partial\varrho}{\partial x_k}, \tag{15}
$$

which includes both the applied electric field and the electrochemical potential gradient.

This approach ensures consistency between the microscopic carrier dynamics and the macroscopic transport coefficients derived, and provides a unified framework for analysing laser-assisted thermomagnetic and Nernst effects in semiconductor superlattices beyond the Landau-quantized regime. Since the representation of Q_i in terms of $\mathcal{E}_k^*$ is not convenient when comparing theory with experiment, it becomes

necessary to express Q_i in terms of J_i and ∇T. Hence,

$$Q_i = \alpha_{ik} T J_k - \kappa_{ik} \nabla_k T, \tag{16}$$

where α_{ik} is the thermomagnetic power tensor, β_{ik} is the thermoelectric tensor, κ_{ik} is the thermal conductivity tensor, $\nabla_k T$ is the temperature gradient, and $\nabla_k \rho$ is the electrochemical potential gradient.

The general component-wise expressions are given as:

$$J_x = \sigma_{xx}\mathcal{E}_x^* + \sigma_{xy}\mathcal{E}_y^* - \beta_{xx}\nabla_x T - \beta_{xy}\nabla_y T, \tag{17}$$

$$J_y = -\sigma_{xy}\mathcal{E}_x^* + \sigma_{yy}\mathcal{E}_y^* + \beta_{xy}\nabla_x T - \beta_{yy}\nabla_y T, \tag{18}$$

$$J_z = \sigma_{zz}\mathcal{E}_z^* - \beta_{zz}\nabla_z T. \tag{19}$$

We explicitly solve the tensorial equations and summarize the carrier conductivity tensor σ_{ik} obtained for the SL under photostimulation and a perpendicular magnetic field, as follows:

$$\sigma_{xx} = \sigma_{\parallel}\left[J_0^2(z\cos\phi) + \frac{1}{2}\Omega\tau z \sin\phi J_1(z\cos\phi)\right] \tag{20}$$

$$\sigma_{xy} = -\sigma_{yx} = \sigma_{\parallel}\Omega\tau J_0^2(z\cos\phi) \tag{21}$$

$$\sigma_{yy} = \sigma_{\perp} = \frac{ne^2\tau}{m^*} \tag{22}$$

where

$$\sigma_{\parallel} = \frac{e^2 n d^2 \tau \Delta}{\hbar}\cdot\frac{I_1(\Delta^*)}{I_0(\Delta^*)}, \quad \Delta^* = \frac{\Delta}{kT}, \quad \omega_c = \frac{e\mathcal{H}}{m^* c}.$$

Thermal averages of velocity-dependent quantities require integrals involving the Boltzmann weight $\exp(\Delta^*\cos x)$, which naturally produce modified Bessel functions I_0 and I_1. For instance averaging v_x within the first Brillouin zone,

$$\langle v_x^2\rangle = \frac{1}{2\pi I_0(\Delta^*)}\int_{-\pi}^{\pi}\sin^2 x\, e^{\Delta^*\cos x}\,dx, \tag{23}$$

and the well-known identity

$$\frac{\int \cos x\, e^{\Delta^*\cos x}\,dx}{\int e^{\Delta^*\cos x}\,dx} = \frac{I_1(\Delta^*)}{I_0(\Delta^*)}. \tag{24}$$

These integrals yield miniband correction terms such as

$$2 + \Delta^*\frac{I_0(\Delta^*)}{I_1(\Delta^*)} + \Delta^{*2} - \Delta^{*2}\left(\frac{I_0(\Delta^*)}{I_1(\Delta^*)}\right)^2, \tag{25}$$

which encode the non-parabolic nature of superlattice transport.

Inserting $F_1(\vec{p})$ into the heat flux expression converts momentum sums into conductivity-weighted averages. The electrical conductivity in the miniband is

$$\sigma_{xx} = \frac{e^2\tau}{kT}\sum_p v_x^2 F_0(\vec{p})(1 - F_0(\vec{p})), \tag{26}$$

so the thermal conductivity assumes a generalized Wiedemann–Franz form : $\kappa_{ik} = \dfrac{\sigma_{ik}k^2T}{e^2} \times$ (miniband correction terms).

Multiple scattering processes are included using Matthiessen's rule [2]:

$$\frac{1}{\tau_{\text{eff}}} = \frac{1}{\tau_0}(1 + \vartheta_1 + \vartheta_2), \tag{27}$$

where

$$\vartheta_1 = \frac{J_o^2(2z\cos\varphi)}{J_o^2(z\cos\varphi)} \qquad \vartheta_2 = \frac{[J_o^2(2z\cos\varphi) + \frac{1}{2}\Omega\tau z\sin\varphi J_1(2z\cos\varphi)]}{[J_o^2(z\cos\varphi) + \frac{1}{2}\Omega\tau z\sin\varphi J_1(2z\cos\varphi)]},$$

which produces different renormalization factors in the longitudinal and transverse transport channels. The parameters ϑ_1 and ϑ_2 arise from the Lorentz force contribution and describe magnetic-field-induced modulation of scattering processes.

The influence of several independent scattering mechanisms on the carrier dynamics is incorporated via Matthiessen's rule. If τ_0 denotes a reference relaxation time for example, due to acoustic phonons, and additional scattering channels introduce relative modifications parametrized by ϑ_1 and ϑ_2, we write Eq. (27) for which small ϑ_i can be linearized as

$$\tau_{\text{eff}} \simeq \tau_0\left(1 - \vartheta_1 - \vartheta_2\right). \tag{28}$$

The choices of which ϑ_i enter a given transport component reflect the physical origin of the scattering for example, processes that preferentially relax momentum along the SL axis contribute to ϑ_2; those that produce transverse relaxation or skew scattering contribute to ϑ_1.

The factors ϑ_1 and ϑ_2 represent phenomenological corrections associated with additional scattering channels beyond the baseline relaxation process. Specifically, θ_1 predominantly renormalizes longitudinal momentum relaxation, whereas θ_2 accounts for the modified transverse response under magnetic deflection and anisotropic scattering.

We acknowledge that the constant relaxation time approximation assumes weak energy dependence of scattering. While this approximation enables analytical solutions, it may not fully capture low-temperature effects where energy-dependent scattering becomes significant: $\tau(\vartheta) \propto \vartheta^r$.

The electrical conductivity components follow directly from the linearized Boltzmann solution. The longitudinal (Drude-like) conductivity along x is

$$\sigma_{xx} = e^2\sum_p v_x^2\,\tau_{\text{eff}}\left(-\frac{\partial F_0(\vec{p})}{\partial\vartheta}\right), \tag{29}$$

where the summation over p is the phase-space integral given as:

$$\sum_p \to \int \frac{d^3p}{(2\pi\hbar)^3}. \tag{30}$$

which after converting the momentum sum to an energy/angle average becomes

$$\sigma_{xx} = \frac{e^2\tau_{\text{eff}}}{kT}\mathcal{N}\,\langle v_x^2\rangle, \tag{31}$$

where $\mathcal{N}$ is an appropriate density-of-states factor and $\langle v_x^2\rangle$ is the miniband average of v_x^2. For the cosine miniband these averages are expressible in terms of modified Bessel functions

$$\langle v_x^2\rangle \propto \frac{1}{I_0(\Delta^*)}\int_{-\pi}^{\pi}\sin^2 x\, e^{\Delta^*\cos x}\,dx \sim F_{xx}(\Delta^*), \tag{32}$$

For the cosine miniband $\vartheta(p) = \Delta\left[1 - \cos(pd/\hbar)\right]$, the carrier velocity is v_x. Introducing the dimensionless variable $x = pd/\hbar$, the squared velocity average becomes

$$\langle v_x^2\rangle = \frac{1}{2\pi\, I_0(\Delta^*)}\left(\frac{\Delta d}{\hbar}\right)^2\int_{-\pi}^{\pi}\sin^2 x\, e^{\Delta^*\cos x}\,dx, \tag{33}$$

where I_n denotes the modified Bessel function of the first kind, $\Delta^* = \Delta/(kT)$ and $F_{xx}(\Delta^*)$ is a compact notation for the resulting combination of I_0 and I_1 [7].

Using the identity $\sin^2 x = \frac{1}{2}\left(1 - \cos 2x\right)$, and the standard integrals

$$\int_{-\pi}^{\pi} e^{\Delta^*\cos x}\,dx = 2\pi I_0(\Delta^*), \qquad \int_{-\pi}^{\pi}\cos(2x)\, e^{\Delta^*\cos x}\,dx = 2\pi I_2(\Delta^*),$$

we obtain

$$\int_{-\pi}^{\pi}\sin^2 x\, e^{\Delta^*\cos x}\,dx = \pi\left[I_0(\Delta^*) - I_2(\Delta^*)\right]. \tag{34}$$

Substituting Eq. (34) into Eq. (33), the longitudinal velocity average simplifies to

$$\langle v_x^2\rangle = \left(\frac{\Delta d}{\hbar}\right)^2\frac{I_0(\Delta^*) - I_2(\Delta^*)}{2\, I_0(\Delta^*)}. \tag{35}$$

It is convenient to define the dimensionless function

$$F_{xx}(\Delta^*) \equiv \frac{I_0(\Delta^*) - I_2(\Delta^*)}{2\, I_0(\Delta^*)}, \tag{36}$$

so that

$$\langle v_x^2\rangle = \left(\frac{\Delta d}{\hbar}\right)^2 F_{xx}(\Delta^*). \tag{37}$$

When a magnetic field $\vec{H}$ is present, the Lorentz force couples velocity components and generates off-diagonal (Hall) response. In the relaxation-time approximation and for weak fields so that $\omega_c\tau_{\rm eff} \ll 1$, where ω_c is the cyclotron frequency relevant to the miniband motion, the transverse conductivity is obtained to leading order as

$$\sigma_{xy} \simeq \sigma_{xx}\,(\omega_c\tau_{\rm eff}) \;+\; \mathcal{O}((\omega_c\tau)^3). \tag{38}$$

Because $\tau_{\rm eff}$ itself contains the ϑ_i corrections [Eq. (28)], one sees immediately that σ_{xy} acquires terms proportional to ϑ_1, those processes that selectively change the transverse relaxation time or introduce skewness, while σ_{xx} is renormalized primarily by ϑ_2, longitudinal momentum-relaxing channels.

Expanding Eqs. (31)–(38) to first order in ϑ_i and isolating the prefactors that depend on miniband geometry gives the linearized forms. Writing the unperturbed (longitudinal) conductivity as

$$\sigma_{xx}^{(0)} \equiv \frac{e^2\tau_0}{kT}\,\mathcal{N}\,F_{xx}(\Delta^*), \tag{39}$$

we obtain to first order

$$\sigma_{xx} \simeq \sigma_{xx}^{(0)}\left(1-\vartheta_2\right), \tag{40}$$

$$\sigma_{xy} \simeq \sigma_{xx}^{(0)}\left(\omega_c\tau_0\right)\left(1-\vartheta_1\right). \tag{41}$$

The precise numerical combination of modified Bessel functions that multiplies ϑ_1 or ϑ_2 in the conductivity and hence in the thermal conductivity via the generalized Wiedemann–Franz relation stems from carrying out the angular integrals in Eq. (32) and related averages such as $\langle v_x^2(\vartheta-\varrho)\rangle$; these produce the characteristic combinations $2+\Delta^*\frac{I_0(\Delta^*)}{I_1(\Delta^*)}+\Delta^{*2}-\Delta^{*2}\big(\frac{I_0(\Delta^*)}{I_1(\Delta^*)}\big)^2$ and its reciprocal forms that appear in the final expressions for κ_{ik}.

Thus, Matthiessen's rule supplies the modified relaxation time, which directly renormalizes the longitudinal conductivity and — through the factor $\omega_c\tau_{\rm eff}$ — the Hall conductivity. The different ways the scattering corrections enter longitudinal and transverse channels via ϑ_2 and ϑ_1, respectively are what ultimately produce the distinct ϑ_i-dependent terms multiplying the bracketed Bessel-function factors in the thermal-conductivity tensor components.

Similarly, using the BTE within the constant relaxation-time and assuming a non-degenerate carrier distribution, the thermoelectric tensor β_{ik} components, we first consider the longitudinal and transverse in-plane components, β_{xx} and β_{xy}, and rewrite them in a compact and systematic form suitable for subsequent tensor inversion. The longitudinal thermoelectric coefficient yields

$$\beta_{xx} = -\frac{k}{e}\,\sigma_{xx}\left[\left(\frac{\Delta-\varrho}{kT}\right) - 3 - \Delta^*\frac{I_0(\Delta^*)}{I_1(\Delta^*)}\right], \tag{42}$$

where Δ is the miniband width, ϱ is the chemical potential measured from the miniband bottom, $\Delta^* = \Delta/(kT)$ is the dimensionless miniband parameter, and I_0 and I_1 are modified Bessel functions of the first kind.

Similarly, the off-diagonal thermoelectric coefficient is

$$\beta_{xy} = -\beta_{yx} = \frac{k}{e}\,\sigma_{xy}\left[\left(\frac{\Delta-\varrho}{kT}\right) - 3 - \Delta^*\frac{I_0(\Delta^*)}{I_1(\Delta^*)}\right]. \tag{43}$$

and the transverse component is also given as

$$\beta_{yy} = -\frac{k}{e}\sigma_{yy}\left[\left(\frac{\Delta-\varrho}{kT}\right) + 2 - \Delta^*\frac{I_1(\Delta^*)}{I_0(\Delta^*)}\right] \tag{44}$$

Eqs. (42)–(44) contain an identical energy–entropy bracket that encapsulates the combined effects of the miniband structure, carrier filling, and thermal averaging. For compactness and clarity, we define

$$\Gamma \equiv \left(\frac{\Delta-\varrho}{kT}\right) - 3 - \Delta^*\frac{I_0(\Delta^*)}{I_1(\Delta^*)}. \tag{45}$$

Using this definition, the thermoelectric tensor components reduce to the compact forms

$$\beta_{xx} = -\frac{k}{e}\,\sigma_{xx}\,\Gamma, \qquad \beta_{xy} = \frac{k}{e}\,\sigma_{xy}\,\Gamma, \qquad \beta_{yx} = -\beta_{xy}. \tag{46}$$

For completeness, Eqs. (42)–(44) and Eq. (46) may also be written explicitly in expanded form as

$$\beta_{xx} = -\frac{k}{e}\sigma_{xx}\left(\frac{\Delta-\varrho}{kT}\right) + \frac{3k}{e}\sigma_{xx} + \frac{k}{e}\sigma_{xx}\Delta^*\frac{I_0(\Delta^*)}{I_1(\Delta^*)}, \tag{47}$$

$$\beta_{xy} = \frac{k}{e}\sigma_{xy}\left(\frac{\Delta-\varrho}{kT}\right) - \frac{3k}{e}\sigma_{xy} - \frac{k}{e}\sigma_{xy}\Delta^*\frac{I_0(\Delta^*)}{I_1(\Delta^*)}, \tag{48}$$

which makes explicit the separate contributions arising from the band offset, entropy term, and miniband thermal correction.

The antisymmetry $\beta_{xy} = -\beta_{yx}$ follows directly from Onsager reciprocity relations and reflects the magnetic-field-induced Hall deflection of carriers. Writing the thermoelectric tensor in the compact form is crucial for the analytical evaluation of the thermomagnetic power tensor α_{ik} under open-circuit conditions. Under open circuit condition $\mathbf{J} = 0$, the thermomagnetic power tensor is defined as

$$\alpha_{ik} = -\sum_j (\sigma^{-1})_{ij}\,\beta_{jk}, \tag{49}$$

which, for the longitudinal component, yields

$$\alpha_{xx} = \frac{\sigma_{yy}\beta_{xx} + \sigma_{xy}\beta_{xy}}{\sigma_{xx}\sigma_{yy} + \sigma_{xy}^2}. \tag{50}$$

Substituting Eqs. (47) and (48) into Eq. (50), we obtain

$$\begin{aligned}\alpha_{xx} &= \frac{1}{\sigma_{xx}\sigma_{yy}+\sigma_{xy}^2}\left[\sigma_{yy}\left(-\frac{k}{e}\sigma_{xx}\Gamma\right) + \sigma_{xy}\left(\frac{k}{e}\sigma_{xy}\Gamma\right)\right] \\ &= -\frac{k}{e}\Gamma\frac{\sigma_{xx}\sigma_{yy}-\sigma_{xy}^2}{\sigma_{xx}\sigma_{yy}+\sigma_{xy}^2}.\end{aligned} \tag{51}$$

This expression shows explicitly that the longitudinal thermomagnetic power is controlled by the competition between longitudinal conductivity σ_{xx} and Hall conductivity σ_{xy}. In the absence of a magnetic field ($\sigma_{xy} \to 0$), the classical Seebeck result is recovered, while finite σ_{xy} introduces a magnetically induced correction that enables a nonzero longitudinal Nernst response.

The compact representation introduced above allows the laser-induced renormalization of the conductivity tensor to be incorporated naturally through dimensionless dressing factors, leading directly to the final expressions for α_{xx}, α_{xy}, and the associated longitudinal and transverse Nernst coefficients.

The thermomagnetic power tensor α_{ik}, also known as the Seebeck coefficient under a magnetic field, describes the link between the temperature gradient and the resulting electric field or current within the system. The thermoelectric response becomes anisotropic and nonlinear in the presence of external fields, such as magnetic and laser-induced electric fields.

The components of the thermomagnetic power tensor were determined from the BTE by applying the kinetic theory of transport in SLs and the semiclassical technique. The expressions depend on several material parameters, and the features of the applied laser and magnetic fields.

Consequently, the longitudinal element of the coefficient is further expressed as:

$$\begin{aligned}\alpha_{xx} &= \frac{1}{\sigma_{xx}\sigma_{yy}+\sigma_{xy}^2}\left(\sigma_{yy}\cdot\left(-\frac{k}{e}\sigma_{xx}\left[\left(\frac{\Delta-\varphi}{kT}\right) - 3 - \Delta^*\frac{I_0(\Delta^*)}{I_1(\Delta^*)}\right]\right)\right. \\ &\left. + \sigma_{xy}\cdot\frac{k}{e}\sigma_{xy}\left[\left(\frac{\Delta-\varphi}{kT}\right) - 3 - \Delta^*\frac{I_0(\Delta^*)}{I_1(\Delta^*)}\right]\right) \\ &= \frac{-(k/e)}{\sigma_{xx}\sigma_{yy}+\sigma_{xy}^2}\left[\left(\frac{\Delta-\varphi}{kT}\right) - 3 - \Delta^*\frac{I_0(\Delta^*)}{I_1(\Delta^*)}\right]\left(\sigma_{xx}\sigma_{yy}-\sigma_{xy}^2\right)\end{aligned} \tag{52}$$

and thus

$$\alpha_{xx} = -\frac{k}{e}\left[\left(\frac{\Delta-\varphi}{kT}\right) - 3 - \Delta^*\frac{I_0(\Delta^*)}{I_1(\Delta^*)}\right]\cdot\left(\frac{\sigma_{xx}\sigma_{yy}-\sigma_{xy}^2}{\sigma_{xx}\sigma_{yy}+\sigma_{xy}^2}\right). \tag{53}$$

The conductivity ratio in the above equation is adjusted or reparametrized with the dimensionless factor ϑ_2 to allow for laser-induced modulation. The longitudinal component of the thermomagnetic power tensor (α_{xx}) is calculated as follows:

$$\alpha_{xx} = -\frac{k}{e}\left\{\left(\frac{\Delta-\varrho}{kT}\right)+1+\left[2-\Delta^*\frac{I_0(\Delta^*)}{I_1(\Delta^*)}\right]\vartheta_2\right\}. \tag{54}$$

This component describes thermomagnetic power along the axis of the SL, including contributions from the energy band structure and laser-induced stimulation via ϑ_2.

The off-diagonal component of the thermomagnetic power ($\alpha_{xy} = -\alpha_{yx}$) can alternatively be calculated as:

$$\alpha_{xy} = -\frac{k}{e}\left\{\left(\frac{\Delta-\varrho}{kT}\right)+1+\left[2-\Delta^*\frac{I_0(\Delta^*)}{I_1(\Delta^*)}\right]\vartheta_1\right\}. \tag{55}$$

The transverse component of the thermomagnetic power (α_{yy}) can be calculated similarly as

$$\alpha_{yy} = -\frac{k}{e}\left\{\frac{3}{2}\cdot\frac{(e\mathcal{E}_1\tau)^2}{m^*kT}+\left(\frac{\Delta-\varrho}{kT}\right)+3-\Delta^*\frac{I_1(\Delta^*)}{I_0(\Delta^*)}\right\}. \tag{56}$$

The intensity of the laser field, as represented by the $(e\mathcal{E}_1\tau)^2$ term, influences the transverse thermomagnetic power, in addition to the energy parameters.

The carrier thermal conductivity tensor κ_{ik} using the BTE follows from the heat flux density as

$$\kappa_{xx} = \frac{\sigma_{xx}k^2T}{e^2}\left\{1-\left[2+\Delta^*\frac{I_0(\Delta^*)}{I_1(\Delta^*)}+\Delta^{*2}-\Delta^{*2}\left(\frac{I_0(\Delta^*)}{I_1(\Delta^*)}\right)^2\right]\vartheta_2\right\}, \tag{57}$$

$$\kappa_{xy} = -\kappa_{yx} = \frac{\sigma_{xx}k^2T}{e^2}\left\{1+\left[2+\Delta^*\frac{I_0(\Delta^*)}{I_1(\Delta^*)}+\Delta^{*2}-\Delta^{*2}\left(\frac{I_0(\Delta^*)}{I_1(\Delta^*)}\right)^2\right]\vartheta_1\right\}, \tag{58}$$

$$\kappa_{yy} = \frac{\sigma_\perp k^2T}{e^2}\left\{2-\Delta^*\frac{I_1(\Delta^*)}{I_0(\Delta^*)}+\Delta^{*2}-\Delta^{*2}\left(\frac{I_1(\Delta^*)}{I_0(\Delta^*)}\right)^2\right\}. \tag{59}$$

In addition to the thermoelectric response, the carrier contribution to the thermal transport plays a crucial role in determining the overall heat flow. Within the semiclassical Boltzmann transport framework and under open-circuit conditions, the electronic thermal conductivity tensor κ_{ik} is obtained from the second-order energy moments of the nonequilibrium distribution function.

In the presence of an external electromagnetic field, photon-assisted transport processes renormalize the carrier dynamics, leading to laser-dressed thermal conductivity components. The longitudinal carrier thermal conductivity is further expanded as

$$\kappa_{xx}^{(L)} = \frac{k^2T}{e^2}\sigma_{xx}^{(L)}\left[\left(\frac{\Delta-\varrho}{kT}\right)^2-6\left(\frac{\Delta-\varrho}{kT}\right)+6+2\Delta^*\frac{I_0(\Delta^*)}{I_1(\Delta^*)}\right], \tag{60}$$

where $\sigma_{xx}^{(L)}$ is the laser-modified longitudinal electrical conductivity and the remaining parameters retain their usual meanings.

Similarly, the off-diagonal component of the carrier thermal conductivity is

$$\kappa_{xy}^{(L)} = -\kappa_{yx}^{(L)} = -\frac{k^2T}{e^2}\sigma_{xy}^{(L)}\left[\left(\frac{\Delta-\varrho}{kT}\right)^2-6\left(\frac{\Delta-\varrho}{kT}\right)+6+2\Delta^*\frac{I_0(\Delta^*)}{I_1(\Delta^*)}\right]. \tag{61}$$

Eqs. (60) and (61) contain an identical quadratic energy-dependent bracket, which reflects the second moment of the carrier energy distribution relative to the chemical potential. For compactness, we define the dimensionless parameter

$$\Lambda \equiv \left(\frac{\Delta-\varrho}{kT}\right)^2-6\left(\frac{\Delta-\varrho}{kT}\right)+6+2\Delta^*\frac{I_0(\Delta^*)}{I_1(\Delta^*)}. \tag{62}$$

Using this definition, the carrier thermal conductivity tensor components reduce to the compact forms

$$\kappa_{xx}^{(L)} = \frac{k^2T}{e^2}\sigma_{xx}^{(L)}\Lambda, \qquad \kappa_{xy}^{(L)} = -\frac{k^2T}{e^2}\sigma_{xy}^{(L)}\Lambda, \qquad \kappa_{yx}^{(L)} = -\kappa_{xy}^{(L)}. \tag{63}$$

For completeness, the fully expanded expressions corresponding to Eqs. (60) and (61) are written as

$$\kappa_{xx}^{(L)} = \frac{k^2T}{e^2}\sigma_{xx}^{(L)}\left(\frac{\Delta-\varrho}{kT}\right)^2-\frac{6k^2T}{e^2}\sigma_{xx}^{(L)}\left(\frac{\Delta-\varrho}{kT}\right)+\frac{6k^2T}{e^2}\sigma_{xx}^{(L)}+\frac{2k^2T}{e^2}\sigma_{xx}^{(L)}\Delta^*\frac{I_0(\Delta^*)}{I_1(\Delta^*)}, \tag{64}$$

$$\kappa_{xy}^{(L)} = -\frac{k^2T}{e^2}\sigma_{xy}^{(L)}\left(\frac{\Delta-\varrho}{kT}\right)^2+\frac{6k^2T}{e^2}\sigma_{xy}^{(L)}\left(\frac{\Delta-\varrho}{kT}\right)-\frac{6k^2T}{e^2}\sigma_{xy}^{(L)}-\frac{2k^2T}{e^2}\sigma_{xy}^{(L)}\Delta^*\frac{I_0(\Delta^*)}{I_1(\Delta^*)}, \tag{65}$$

with $\kappa_{yx}^{(L)} = -\kappa_{xy}^{(L)}$ following directly from Onsager reciprocity relations.

The quadratic dependence on $(\Delta-\varrho)/(kT)$ reflects the dominant role of energy fluctuations in thermal transport, while the Bessel-function term encapsulates the influence of miniband dispersion and thermal averaging. The antisymmetric transverse component arises from magnetic-field-induced carrier deflection and is responsible for the transverse heat flow associated with the thermal Hall and Nernst effects.

In the limit of vanishing electromagnetic radiation, $\sigma_{ik}^{(L)} \to \sigma_{ik}$, the expressions in Eq. (60) reduce smoothly to their field-free counterparts, demonstrating that the laser field acts as an external control parameter for tuning both longitudinal and transverse carrier thermal conductivities in semiconductor superlattices.

Moreover, the Ettingshausen effect describes the generation of a transverse temperature gradient in a conductor when an electric current flows in the presence of a magnetic field. The corresponding Ettingshausen coefficient quantifies this thermal response per unit magnetic field and current density.

The Ettingshausen coefficient is defined by:

$$\nabla_i T = \mathcal{P}_{ik}\mathcal{H}J_k \quad \Rightarrow \quad \mathcal{P}_{ik} = \frac{1}{\mathcal{H}}\cdot\frac{\nabla_i T}{J_k} \tag{66}$$

In the linear thermomagnetic transport regime, from the heat current relation: $Q_i = \alpha_{ik}TJ_k - \kappa_{ik}\nabla_k T$. Assuming an adiabatic condition ($Q_i = 0$), we solve for $\nabla_k T$:

$$\nabla_k T = \kappa_{ik}^{-1}\alpha_{im}TJ_m \tag{67}$$

Therefore, the Ettingshausen tensor is:

$$\mathcal{P}_{ik} = \frac{T}{\mathcal{H}}\left(\kappa^{-1}\alpha\right)_{ik} \tag{68}$$

Assuming current along the x-direction, magnetic field along z, and temperature gradient along y, defines the transverse Ettingshausen coefficient $\mathcal{P}_y$ as:

$$\mathcal{P}_y = \frac{T}{\mathcal{H}}\cdot\frac{\alpha_{yx}}{\kappa_{yy}} = -\frac{T}{\mathcal{H}}\cdot\frac{\alpha_{xy}}{\kappa_{yy}} \tag{69}$$

Using the expression from the theory:

$$\alpha_{xy} = -\frac{k}{e}\left[\left(\frac{\Delta-\varrho}{kT}\right)+1+\left(2-\Delta^*\frac{I_0(\Delta^*)}{I_1(\Delta^*)}\right)\vartheta_1\right]$$

$$\kappa_{yy} = \frac{\sigma_\perp k^2T}{e^2}\left[2-\Delta^*\frac{I_1(\Delta^*)}{I_0(\Delta^*)}+\Delta^{*2}-\Delta^{*2}\left(\frac{I_1(\Delta^*)}{I_0(\Delta^*)}\right)^2\right]$$

Hence:

$$\mathcal{P}_y = \frac{T}{\mathcal{H}}\cdot\frac{k}{e\kappa_{yy}}\left[\left(\frac{\Delta-\varrho}{kT}\right)+1+\left(2-\Delta^*\frac{I_0(\Delta^*)}{I_1(\Delta^*)}\right)\vartheta_1\right] \tag{70}$$

Similarly, the longitudinal Ettingshausen coefficient $\mathcal{P}_x$ becomes:

$$\mathcal{P}_x = \frac{T}{\mathcal{H}}\cdot\frac{\alpha_{xy}}{\kappa_{xx}} \tag{71}$$

where

$$\kappa_{xx} = \frac{\sigma_{xx}k^2T}{e^2}\left\{1-\left[2+\Delta^*\frac{I_0(\Delta^*)}{I_1(\Delta^*)}+\Delta^{*2}-\Delta^{*2}\left(\frac{I_0(\Delta^*)}{I_1(\Delta^*)}\right)^2\right]\vartheta_2\right\}.$$

Substituting into $\mathcal{P}_x$ yields:

$$\mathcal{P}_x = -\frac{T}{\mathcal{H}}\cdot\frac{\alpha_{xy}}{\kappa_{xx}} = \frac{T}{\mathcal{H}}\cdot\frac{k}{e\kappa_{xx}}\left[\left(\frac{\Delta-\varrho}{kT}\right)+1+\left(2-\Delta^*\frac{I_0(\Delta^*)}{I_1(\Delta^*)}\right)\vartheta_1\right] \tag{72}$$

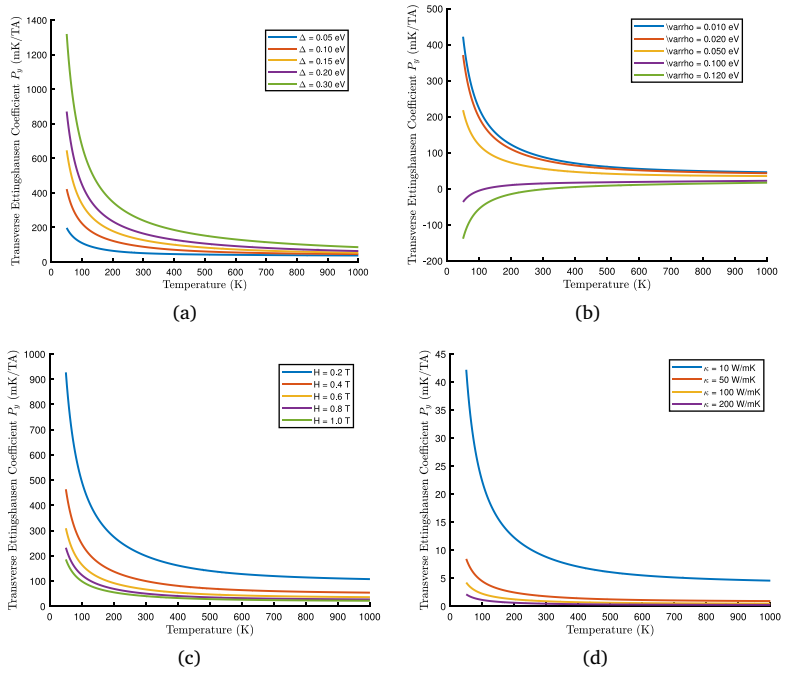

Fig. 2. Dependency of transverse Ettingshausen coefficient ($\mathcal{P}_y$) on temperature (T) for varied values of: (a) Δ with $n_o = 10^{18}$ cm^{-3}, and $\mathcal{E}_1 = 10^5$ V/m; (b) ϱ with $\Delta = 0.10$ eV, $n_o = 10^{18}$ cm^{-3}, and $\mathcal{E}_1 = 10^5$ V/m; (c) $\mathcal{H}$ with $\Delta = 0.10$ eV, $n_o = 10^{18}$ cm^{-3}, $\mathcal{E}_1 = 10^5$ V/m; (d) κ_{yy} with $\Delta = 0.10$ eV, $n_o = 10^{18}$ cm^{-3}, and $\mathcal{E}_1 = 10^5$ V/m.

The Ettingshausen and Nernst effects are reciprocal thermomagnetic phenomena. In the weak-field linear regime, the two coefficients are proportional through the thermal conductivity and temperature, implying that sign reversals predicted for the Ettingshausen coefficient should be mirrored in the corresponding Nernst response.

By Onsager reciprocity, $\alpha_{xy}(\mathcal{H}) = \alpha_{yx}(-\mathcal{H})$, the Nernst coefficient is defined as $\nu = -\dfrac{\mathcal{E}_y}{(\nabla_x T)\mathcal{H}}$, while the Ettingshausen coefficient is $\mathcal{P} = \dfrac{\nabla_y T}{J_x \mathcal{H}}$.

Under linear response,

$$\mathcal{P} = \frac{T}{\kappa}\nu, \tag{73}$$

up to tensor corrections.

3. Results and discussion

It is critical to distinguish the Ettingshausen effect outlined above from the similarly related Nernst effect. The Nernst effect uses an applied temperature gradient to generate a transverse electric field in a magnetic field, whereas the Ettingshausen effect uses an applied electric current to create a transverse temperature gradient in a magnetic field. The two events are thermodynamically conjugate and related by Onsager reciprocity connections, although their physical manifestations show separate transport paths. This study focusses on the Ettingshausen effect in superlattices, demonstrating how the interplay of electronic miniband structure, external fields, and thermal transport coefficients governs transverse thermal responses induced by electric currents, complementing previous studies of the Nernst effect in low-dimensional systems.

The non-monotonic temperature dependence arises from the competition between diagonal and off-diagonal transport tensors entering the Ettingshausen coefficient. Because σ_{ij} and S_{ij} respond differently to temperature, magnetic field, and chemical potential, their relative balance can change sign, leading to extrema and zero crossings. Thermal broadening at higher temperature suppresses this sensitivity and produces saturation.

Fig. 2 present the dependency of transverse Ettingshausen coefficient ($\mathcal{P}_y$) on temperature (T) for varied values of: (a) Δ with $n_o = 10^{18}$ cm^{-3}, and $\mathcal{E}_1 = 10^5$ V/m; (b) ϱ with $\Delta = 0.10$ eV, $n_o = 10^{18}$ cm^{-3}, and $\mathcal{E}_1 = 10^5$ V/m; (c) $\mathcal{H}$ with $\Delta = 0.10$ eV, $n_o = 10^{18}$ cm^{-3}, $\mathcal{E}_1 = 10^5$ V/m; and (d) κ_{yy} with $\Delta = 0.10$ eV, $n_o = 10^{18}$ cm^{-3}, and $\mathcal{E}_1 = 10^5$ V/m.

In Fig. 2a discuss the $\mathcal{P}_y$ variation of miniband width Δ on temperature. Increasing Δ raises $\Delta^* = \Delta/(kT)$ at a given temperature. For small Δ, the curves show a smooth positive plateau. For large Δ, the denominator $F(\Delta^*)$ decreases and may change sign, while $\mathcal{B}$ grows. This produces the strong growth and a possible sign change at low temperatures. Physically, a wider miniband increases electronic energy scales and modifies the density of states, producing a stronger low-temperature response. In particular, $\mathcal{P}_y$ is obtained in Eq. (70) where $\vartheta_1 = J_0^2(2z\cos\phi)/J_0^2(z\cos\phi)$ encodes the influence of the ac field. Simplifying Eq. (70) yields

$$\mathcal{P}_y = \frac{e}{\sigma_\perp k\mathcal{H}F(\Delta^*)}\,\mathcal{B}(\Delta^*, \varrho, T), \tag{74}$$

where

$$F(\Delta^*) = 2 - \Delta^*\frac{I_1}{I_0} + \Delta^{*2} - \Delta^{*2}\left(\frac{I_1(\Delta^*)}{I_0(\Delta^*)}\right)^2, \tag{75}$$

$$\mathcal{B} = \frac{\Delta - \varrho}{kT} + 1 + \left(2 - \Delta^*\frac{I_0(\Delta^*)}{I_1(\Delta^*)}\right)\vartheta_1. \tag{76}$$

Thus,

$$\mathcal{P}_y \propto \frac{1}{\sigma_\perp}\cdot\frac{1}{\mathcal{H}}\cdot\frac{\mathcal{B}}{F(\Delta^*)}. \tag{77}$$

All the temperature dependence is implicit via $\Delta^* = \Delta/(kT)$ and via the explicit $\varrho/(kT)$ term. In the asymptotic limits, for small Δ^* (high temperature), using $I_0(\Delta^*) \approx 1 + \Delta^{*2}/4$, $I_1(\Delta^*) \approx \Delta^*/2$, one finds $I_1(\Delta^*)/I_0(\Delta^*) \approx \Delta^*/2$, $I_0(\Delta^*)/I_1(\Delta^*) \approx 2/\Delta^*$. Then

$$F(\Delta^*) \approx 2 + \frac{\Delta^{*2}}{2}, \qquad 2 - \Delta^*\frac{I_0(\Delta^*)}{I_1(\Delta^*)} \approx 0.$$

Therefore

$$\mathcal{B} \approx 1 - \frac{\varrho}{kT}, \qquad \mathcal{P}_y \approx \frac{e}{2\sigma_\perp k\mathcal{H}}\left(1 - \frac{\varrho}{kT}\right).$$

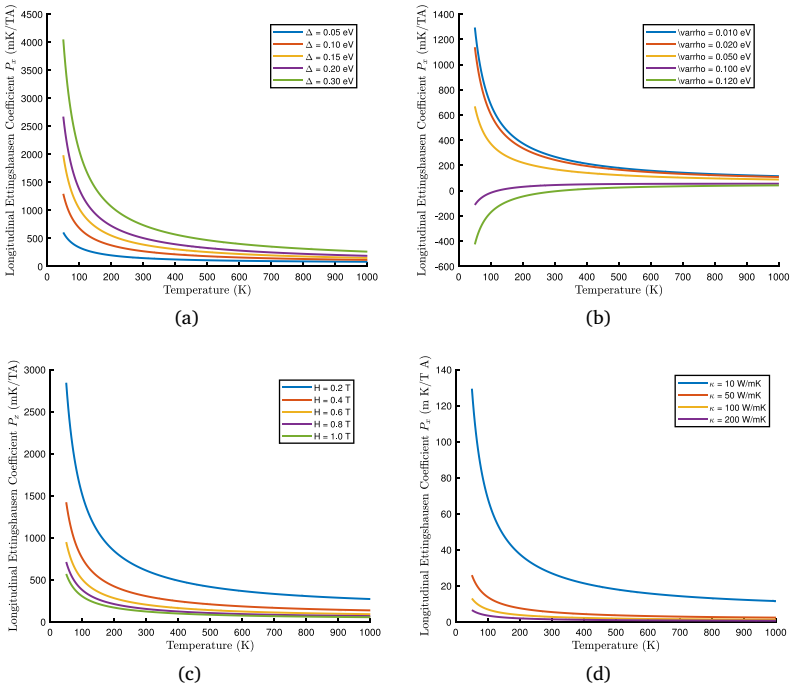

Fig. 3. Dependency of longitudinal Ettingshausen coefficient ($\mathcal{P}_x$) on temperature (T) for varied values of: (a) Δ with $n_o = 10^{18}$ cm^{-3}, and $\mathcal{E}_1 = 10^5$ V/m; (b) ϱ with $\Delta = 0.10$ eV, $n_o = 10^{18}$ cm^{-3}, and $\mathcal{E}_1 = 10^5$ V/m; (c) $\mathcal{H}$ with $\Delta = 0.10$ eV, $n_o = 10^{18}$ cm^{-3}, $\mathcal{E}_1 = 10^5$ V/m; (d) κ_{xx} with $\Delta = 0.10$ eV, $n_o = 10^{18}$ cm^{-3}, and $\mathcal{E}_1 = 10^5$ V/m.

At high temperatures, $\mathcal{P}_y$ is nearly constant and positive, with a small correction from $\varrho/(kT)$.

However, when large Δ^* (low temperature). For $\Delta^* \gg 1$, $I_1(\Delta^*)/I_0(\Delta^*) \to 1$, so

$$F(\Delta^*) \approx 2 - \Delta^*,$$

while $\mathcal{B} \sim \dfrac{\Delta - \varrho}{kT} + \cdots = \Delta^* - \dfrac{\varrho}{kT} + \cdots$.

Thus at low temperature, $\mathcal{B}$ grows as Δ^*, while $F(\Delta^*)$ can become small or negative. The ratio $\mathcal{B}/F$ may therefore change sign, leading to peaks or zero-crossings in $\mathcal{P}_y$.

In Fig. 2b, we display the variation of chemical potential ϱ dependence on temperature. ϱ enters linearly as $-\varrho/(kT)$ in $\mathcal{B}$ and increasing ϱ shifts $\mathcal{B}$ downward, making $\mathcal{P}_y$ smaller and possibly negative at low temperature. At high temperature, $\varrho/(kT)$ is small and all curves converge. Negative low-temperature values occur when ϱ is sufficiently large compared to Δ.

The variation of the magnetic field $\mathcal{H}$ on the transverse Ettingshausen coefficient is displayed in Fig. 2c. From the prefactor, $\mathcal{P}_y \propto 1/\mathcal{H}$. Thus, higher fields reduce the magnitude of $\mathcal{P}_y$. In this formulation, ϑ_1 is field-independent, so the $1/\mathcal{H}$ scaling is the dominant effect. Physically, a larger $\mathcal{H}$ suppresses the transverse temperature gradient per current density.

Moreover, Fig. 2d describes the variation of thermal conductivity κ_{yy}. Since $\mathcal{P}_y = (T/\mathcal{H})(\alpha_{yx}/\kappa_{yy})$, increasing κ_{yy} directly decreases $\mathcal{P}_y$. A larger thermal conductivity diffuses heat more efficiently, reducing the measurable temperature gradient per unit current and field.

$\mathcal{P}_y$ scales inversely with $\sigma_\perp$, $\mathcal{H}$, and κ_{yy}. Temperature dependence arises from the competition between the numerator $\mathcal{B}(\Delta^*, \varrho, T)$ and denominator $F(\Delta^*)$. At high temperature, $\mathcal{P}_y$ is positive and weakly dependent on parameters, and at low temperature, non-monotonic behaviour and sign changes appear due to Δ^* dependence and the $\varrho/(kT)$ shift.

We present in Fig. 3 the dependency of longitudinal Ettingshausen coefficient ($\mathcal{P}_x$) on temperature (T) for varied values of: (a) Δ with $n_o = 10^{18}$ cm^{-3}, and $\mathcal{E}_1 = 10^5$ V/m; (b) ϱ with $\Delta = 0.10$ eV, $n_o = 10^{18}$ cm^{-3}, and $\mathcal{E}_1 = 10^5$ V/m; (c) $\mathcal{H}$ with $\Delta = 0.10$ eV, $n_o = 10^{18}$ cm^{-3}, $\mathcal{E}_1 = 10^5$ V/m; (d) κ_{xx} with $\Delta = 0.10$ eV, $n_o = 10^{18}$ cm^{-3}, and $\mathcal{E}_1 = 10^5$ V/m.

From Eq. (72), the explicit temperature cancels, leaving

$$\mathcal{P}_x = \frac{e}{\sigma_{xx} k\mathcal{H}\, G(\Delta^*, \vartheta_2)}\, \mathcal{N}(\Delta^*, \varrho, \vartheta_1), \tag{78}$$

where

$$G(\Delta^*, \vartheta_2) = 1 - \left[2 + \Delta^* \frac{I_0(\Delta^*)}{I_1(\Delta^*)} + \Delta^{*2} - \Delta^{*2}\left(\frac{I_0(\Delta^*)}{I_1(\Delta^*)}\right)^2\right]\vartheta_2, \tag{79}$$

$$\mathcal{N}(\Delta^*, \varrho, \vartheta_1) = \frac{\Delta - \varrho}{kT} + 1 + \left(2 - \Delta^* \frac{I_0(\Delta^*)}{I_1(\Delta^*)}\right)\vartheta_1. \tag{80}$$

Thus,

$$\mathcal{P}_x \propto \frac{1}{\sigma_{xx}} \cdot \frac{1}{\mathcal{H}} \cdot \frac{\mathcal{N}}{G}.$$

Asymptotically for high temperature ($\Delta^* \ll 1$), then $I_0 \approx 1 + \Delta^{*2}/4$, $I_1 \approx \Delta^*/2$, one finds $I_0(\Delta^*)/I_1(\Delta^*) \approx 2/\Delta^*$. Hence

$$2 - \Delta^* \frac{I_0(\Delta^*)}{I_1(\Delta^*)} \approx 0, \quad G \approx 1 - 2\vartheta_2, \quad \mathcal{N} \approx 1 - \frac{\varrho}{kT}.$$

Therefore, $\mathcal{P}_x$ approaches a constant plateau, positive provided $\varrho < kT$.

At low temperature ($\Delta^* \gg 1$), as $I_1(\Delta^*)/I_0(\Delta^*) \to 1$, $I_0(\Delta^*)/I_1(\Delta^*) \to 1$, we have

$$\mathcal{N} \sim \Delta^* - \frac{\varrho}{kT}, \qquad G \sim 1 - (2 + \Delta^*)\vartheta_2.$$

Thus, the numerator grows with Δ^* while the denominator may pass through zero. This competition yields strong low-temperature peaks and possible sign reversals in $\mathcal{P}_x$.

Fig. 3a shows the variation of the carrier miniband width Δ. Larger Δ increases Δ^* at fixed temperature, pushing the system into the low-temperature asymptotic regime. This enhances the numerator $\mathcal{N}$ while potentially driving G negative. The result is amplified response and possible sign changes at low temperature, whereas all curves converge at high temperature.

In Fig. 3b, we display the variation of the chemical potential ϱ. ϱ enters linearly as $-\varrho/(kT)$ in $\mathcal{N}$, and increasing ϱ depresses $\mathcal{N}$, producing downward shifts of $\mathcal{P}_x$. At low temperature this term dominates, leading to negative $\mathcal{P}_x$ for sufficiently large ϱ. At high temperature, the effect vanishes and curves collapse. The observed anomalies arise from the combined effects of:

- Miniband nonlinearity: $v_x \propto \sin(\frac{p_x d}{\hbar})$,
- AC field modulation: $\Delta_{\text{eff}} = \Delta J_0(z), \quad z = \frac{e\mathcal{E}_1 d}{\hbar\omega}$,
- Low-temperature limit: $\frac{\partial F_0}{\partial \vartheta} \to \delta(\vartheta - \varrho)$.

These effects lead to sharp features and non-monotonic behaviour in the Ettingshausen coefficient.

The variation with the magnetic field $\mathcal{H}$ is discussed in Fig. 3c. $\mathcal{P}_x$ contains an explicit $1/\mathcal{H}$ factor. Larger $\mathcal{H}$ therefore suppresses the amplitude. Additionally, ϑ_2 contains $\Omega\tau \propto \mathcal{H}$, altering $G(\Delta^*, \vartheta_2)$. This introduces nonlinear $\mathcal{H}$-dependence beyond the simple inverse scaling, modifying both shape and magnitude of the curves.

In Fig. 3d, we show the variation of the longitudinal thermal conductivity κ_{xx}. Since $\mathcal{P}_x \propto 1/\kappa_{xx}$, increasing κ_{xx} reduces the coefficient. Physically, greater thermal conductivity enhances heat diffusion and diminishes the measurable transverse temperature gradient per unit current and field.

Thus, $\mathcal{P}_x$ is controlled by the ratio $\mathcal{N}/G$, both strongly temperature-dependent via $\Delta^* = \Delta/(kT)$, at high temperature, $\mathcal{P}_x$ saturates to a positive plateau, weakly dependent on parameters, at low temperature, non-monotonicity and sign changes occur due to competition between $\mathcal{N}$ and G, and Increasing Δ amplifies the low-temperature effect, increasing ϱ shifts curves downward, raising H suppresses the magnitude while modifying the shape, and increasing λ_{xx} reduces $\mathcal{P}_x$ inversely.

In practical superlattices, the total thermal conductivity contains both electronic and phononic parts, $\kappa = \kappa_e + \kappa_{ph}$. Therefore, the inverse scaling of the Ettingshausen coefficient should be interpreted with respect to the total thermal conductivity. Neglecting κ_{ph} may overestimate the absolute magnitude of the effect, although the qualitative dependencies on field, temperature, and chemical potential remain unchanged.

3.1. Comparison with other models:

First-principles (DFT-based) methods compute band structures and scattering inputs from

$$H\psi_n = \vartheta_n(\mathbf{k})\psi_n, \tag{81}$$

and are typically used to obtain:

- miniband widths,
- effective masses,
- density of states,
- electron–phonon coupling strengths.

In contrast, our model uses a parametrized miniband dispersion of the form $\vartheta(k_z) = \frac{\Delta}{2}\left[1 - \cos(k_z d)\right]$, which is consistent with tight-binding descriptions of GaAs/AlGaAs superlattices.

The key advantage of the present approach is that it allows: closed-form expressions for thermomagnetic coefficients, explicit dependence on magnetic field and AC driving, and efficient parametric studies over wide phase space.

We now clarify that our results are in qualitative agreement with first-principles trends reported in low-dimensional semiconductor systems, particularly regarding: miniband narrowing effects, enhancement of thermoelectric response in reduced dimensions, and sensitivity of transport coefficients to band curvature.

In summary, while first-principles (DFT-based) methods provide accurate electronic structure information, including miniband widths and effective masses, the present study adopts a semiclassical Boltzmann transport framework with a tight-binding miniband dispersion. This approach enables analytical insight into thermomagnetic transport and efficient exploration of field-dependent behaviour. The resulting trends are consistent with first-principles predictions for low-dimensional semiconductor superlattices, particularly regarding enhanced transport anisotropy and miniband-controlled thermoelectric response.

4. Conclusion

This study has developed a theoretical framework for the Ettingshausen effect in semiconductor superlattices subjected to combined dc–ac electric fields and a magnetic field, using the Boltzmann transport equation. Explicit forms of the longitudinal and transverse Ettingshausen coefficients were obtained, showing that their behaviour is strongly governed by the miniband width, chemical potential, magnetic field, and thermal conductivity.

Our findings demonstrate that both $\mathcal{P}_x$ and $\mathcal{P}_y$ have a strong temperature dependence: at high temperatures, they saturate to finite positive values, whereas at low temperatures, they exhibit amplified responses and even sign reversals depending on the parameter regime. Wider miniband widths increase the low-temperature coefficient, whereas greater chemical potentials decrease it, and stronger magnetic fields and thermal conductivities reduce its total magnitude. These findings emphasize the delicate balance between band structure effects and external control parameters in thermomagnetic transfer.

Thus, the Ettingshausen effect in superlattices is highly adjustable, providing potential to create thermomagnetic responses in nanoscale systems. The findings suggest potential applications in heat management, magnetic field sensing, and energy conversion, as well as motivation for future research involving quantum confinement, nonparabolic dispersion, and experimental verification.

The present analysis focuses on the lowest miniband with isotropic in-plane mass. Occupation of higher minibands or anisotropic transverse masses would quantitatively alter the transport coefficients, particularly at elevated temperatures, but the main mechanism of field-tunable thermomagnetic response remains unchanged.

CRediT authorship contribution statement

D. Sekyi-Arthur: Writing – review & editing, Writing – original draft, Visualization, Validation, Supervision, Software, Resources, Project administration, Methodology, Investigation, Funding acquisition, Formal analysis, Data curation, Conceptualization. **S.Y. Mensah:** Writing – review & editing, Visualization, Methodology, Investigation. **K.A. Dompreh:** Software, Resources.

Declaration of competing interest

The authors declare no conflict of interest in processing this manuscript.

Appendix. Derivation of the Ettingshausen coefficient in GaAs/AlGaAs superlattices under DC–AC fields

This Appendix presents the detailed derivation of the analytical expressions used in the main text for the Ettingshausen coefficient of a semiconductor superlattice subjected to crossed electric and magnetic fields. The treatment is based on the semiclassical Boltzmann transport equation within the relaxation-time approximation.

A.1. Miniband dispersion relation

For electron motion along the growth direction z, the lowest miniband in a GaAs/AlGaAs superlattice is described by the tight-binding form

$$\vartheta(\mathbf{k}) = \frac{\Delta}{2}\left[1 - \cos(k_z d)\right] + \frac{\hbar^2 k_x^2}{2m^*} + \frac{\hbar^2 k_y^2}{2m^*}, \tag{A.1}$$

where:

- Δ is the miniband width,
- d is the superlattice period,
- m^* is the in-plane effective mass.

The carrier velocity components are

$$v_x = \frac{\hbar k_x}{m^*}, \qquad v_y = \frac{\hbar k_y}{m^*}, \tag{A.2}$$

and

$$v_z = \frac{1}{\hbar}\frac{\partial \vartheta}{\partial k_z} = \frac{\Delta d}{2\hbar}\sin(k_z d). \tag{A.3}$$

A.2. Semiclassical equation of motion

Under an electric field

$$\mathcal{E}(t) = \mathcal{E}_{dc}\hat{z} + \mathcal{E}_{ac}\cos(\omega t)\hat{z},$$

and magnetic field

$$\mathbf{H} = H\hat{x},$$

the crystal momentum obeys

$$\hbar\frac{d\mathbf{k}}{dt} = -e\left[\mathbf{E}(t) + \mathbf{v}\times\mathbf{H}\right]. \tag{A.4}$$

For the longitudinal component,

$$\hbar\frac{dk_z}{dt} = -e\left[\mathcal{E}_{dc} + \mathcal{E}_{ac}\cos(\omega t)\right]. \tag{A.5}$$

Integrating gives

$$k_z(t) = k_{z0} - \frac{e\mathcal{E}_{dc}}{\hbar}t - \frac{e\mathcal{E}_{ac}}{\hbar\omega}\sin(\omega t). \tag{A.6}$$

A.3. Boltzmann transport equation

The nonequilibrium distribution function $f(\mathbf{k}, t)$ satisfies

$$\frac{\partial F}{\partial t} + \mathbf{v}\cdot\nabla_{\mathbf{r}}F + \frac{e}{\hbar}(\mathbf{E} + \mathbf{v}\times\mathbf{B})\cdot\nabla_{\mathbf{k}}F = -\frac{F - F_0}{\tau}, \tag{A.7}$$

where F_0 is the Fermi–Dirac equilibrium distribution and τ is the relaxation time.

For weak perturbations, write

$$F = F_0 + F_1, \qquad |F_1| \ll F_0. \tag{A.8}$$

Linearization gives

$$F_1 = -\tau\left[\mathbf{v}\cdot\nabla_{\mathbf{r}}F_0 + \frac{e}{\hbar}(\mathbf{E} + \mathbf{v}\times\mathbf{B})\cdot\nabla_{\mathbf{k}}F_0\right]. \tag{A.9}$$

A.4. Current density and heat flux

The electric current density is

$$\mathbf{J} = -e\int\frac{d^3k}{(2\pi)^3}\,\mathbf{v}F_1. \tag{A.10}$$

The heat current density is

$$\mathbf{Q} = \int\frac{d^3k}{(2\pi)^3}(\vartheta - \varrho)\mathbf{v}F_1. \tag{A.11}$$

These lead to the coupled transport equations

$$J_i = \sum_j \sigma_{ij}\mathcal{E}_j - \sum_j \alpha_{ij}\nabla_j T, \tag{A.12}$$

$$Q_i = \sum_j \Pi_{ij}J_j - \sum_j \kappa_{ij}\nabla_j T. \tag{A.13}$$

A.5. Conductivity tensor in weak magnetic field

For weak magnetic field ($\omega_c\tau \ll 1$),

$$\sigma_{xx} = \frac{\sigma_0}{1 + (\omega_c\tau)^2}, \tag{A.14}$$

$$\sigma_{xy} = \frac{\sigma_0\omega_c\tau}{1 + (\omega_c\tau)^2}, \tag{A.15}$$

where

$$\omega_c = \frac{eB}{m^*}. \tag{A.16}$$

A.6. Thermoelectric tensor

Using transport moments,

$$\mathcal{L}_n = \int d\vartheta\,(\vartheta - \varrho)^n\left(-\frac{\partial F_0}{\partial\vartheta}\right)\Sigma(\vartheta), \tag{A.17}$$

the Seebeck tensor is

$$S_{ij} = \frac{1}{eT}\frac{\mathcal{L}_{1,ij}}{\mathcal{L}_{0,ij}}. \tag{A.18}$$

The electronic thermal conductivity is

$$\kappa_{ij} = \frac{1}{e^2T}\left(\mathcal{L}_{2,ij} - \frac{\mathcal{L}_{1,ij}^2}{\mathcal{L}_{0,ij}}\right). \tag{A.19}$$

A.7. Ettingshausen coefficient

The Ettingshausen effect describes a transverse temperature gradient generated by electric current in a magnetic field:

$$P = \frac{\nabla_y T}{J_x\mathcal{H}}. \tag{A.20}$$

Under open-circuit transverse conditions, one obtains

$$P = \frac{\sigma_{xy}S_{xx} - \sigma_{xx}S_{xy}}{\mathcal{H}\kappa}. \tag{A.21}$$

This is the working expression used in the manuscript.

A.8. High-temperature limit

When $kT \gg \Delta, \varrho$, the derivative of the Fermi function broadens strongly and the transport moments scale as

$$\mathcal{L}_n \propto T^n. \tag{A.22}$$

Hence,

$$P(T) \to \text{constant}, \tag{A.23}$$

which explains the saturation reported in the main text.

A.9. Low-temperature sign reversal

At low temperature, only states near the Fermi level contribute:

$$-\frac{\partial F_0}{\partial\vartheta} \approx \delta(\vartheta - \varrho). \tag{A.24}$$

Therefore,

$$P \propto \left.\frac{d\ln\Sigma(\vartheta)}{d\vartheta}\right|_{\varepsilon=\mu}. \tag{A.25}$$

Changes in miniband curvature or chemical potential can reverse the sign of this derivative, leading to the observed sign reversals.

A.10. Effect of AC field

Using the Jacobi–Anger expansion,

$$e^{iz\sin\omega t} = \sum_{n=-\infty}^{\infty} J_n(z)e^{in\omega t}, \tag{A.26}$$

the time-averaged current contains photon-assisted sidebands weighted by $J_n^2(z)$, where

$$z = \frac{e\mathcal{E}_{ac}d}{\hbar\omega}. \tag{A.27}$$

Thus, the ac field dynamically renormalizes the Ettingshausen response.

A.11. Total thermal conductivity

If phonons are included,

$$\kappa = \kappa_e + \kappa_{ph}. \tag{A.28}$$

Hence,

$$P \propto \frac{1}{\kappa_e + \kappa_{ph}}, \tag{A.29}$$

so neglecting κ_{ph} overestimates the absolute magnitude of the effect.

Data availability

Data will be made available on request.

References

[1] E.H. Sondheimer, The theory of the galvanomagnetic and thermomagnetic effects in metals, Proc. R. Soc. Lond. A 193 (1948) 484–512.
[2] J.M. Ziman, Principles of the Theory of Solids, second ed., Cambridge University Press, 1972.
[3] H.J. Goldsmid, Electronic Refrigeration, Pion Ltd., 1986.
[4] Y.N. Obraztsov, Thermomagnetic effects in semiconductors, Sov. Phys. Solid State 6 (1964) 331–335.
[5] K. Behnia, The Nernst effect and the boundaries of the Fermi liquid picture, J. Phys. : Condens. Matter 21 (11) (2009) 113101.
[6] A. Varlamov, A. Galda, Nernst and Ettingshausen effects: A review, Low Temp. Phys. 35 (12) (2009) 904–916.
[7] L. Esaki, R. Tsu, Superlattice and negative differential conductivity in semiconductors, IBM J. Res. Dev. 14 (1970) 61–65.
[8] J. Bass, Thermoelectricity in metallic multilayers, J. Magn. Magn. Mater. 165 (1997) 19–26.
[9] K. Tanaka, F. Nori, Nernst and Ettingshausen effects in semiconductor superlattices, Phys. Rev. B 44 (7) (1991) 3622–3630.
[10] L.D. Hicks, M.S. Dresselhaus, Effect of quantum-well structures on the thermoelectric figure of merit, Phys. Rev. B 47 (19) (1993) 12727–12731.
[11] M.S. Dresselhaus, et al., New directions for low-dimensional thermoelectric materials, Adv. Mater. 11 (21) (1999) 1749–1751.
[12] D. Sekyi-Arthur, S.Y. Mensah, K.A. Dompreh, F. Amo-Mensah, Thermomagnetic transport and field-tunable figures of merit in GaAs/AlGaAs superlattices, Micro Nanostructures (2026) 208583.
[13] S.Y. Mensah, G.K. Kangah, The thermoelectric effect in a semiconductor superlattice in a non-quantized electric field, J. Phys.: Condens. Matter. 4 (3) (1992) 919.
[14] S.Y. Mensah, P.K. Buah-Bassuah, The thermomagnetic effect in a semiconductor superlattice in the presence of laser radiation, J. Phys.: Condens. Matter 5 (9) (1993) 1349.
[15] J. Shah, Ultrafast Spectroscopy of Semiconductors and Semiconductor Nanostructures, second ed., Springer, 2005.
[16] V. Karavolas, R.A. Abram, Transport in semiconductor superlattices: Effects of miniband parameters, Semicond. Sci. Technol. 14 (11) (1999) 923–931.
[17] K. Seeger, Semiconductor Physics: An Introduction, ninth ed., Springer, 2002.
[18] C.J. Vineis, A. Shakouri, A. Majumdar, M.G. Kanatzidis, Nanostructured thermoelectrics: Big efficiency gains from small features, Adv. Mater. 22 (36) (2010) 3970–3980.
[19] G.J. Snyder, E.S. Toberer, Complex thermoelectric materials, Nat. Mater. 7 (2008) 105–114.
[20] A. Majumdar, Thermoelectricity in semiconductor nanostructures, Science 303 (2004) 777–778.
[21] T.C. Harman, P.J. Taylor, M.P. Walsh, B.E. LaForge, Quantum dot superlattice thermoelectric materials and devices, Science 297 (5590) (2002) 2229–2232.
[22] F.G. Bass, A.P. Tetervov, High-Frequency Properties of Semiconductor Superlattices, Springer, New York, 1986.
[23] D. Sekyi-Arthur, S.Y. Mensah, K.A. Dompreh, G. Nkrumah-Buandoh, N.G. Mensah, Giant thermoelectric power in fluorine-doped single-walled carbon nanotubes, J. Phys. Chem. Solids 171 (2022) 111020.
[24] D. Sekyi-Arthur, C. Jebuni-Adanu, S.Y. Mensah, E.K. Amewude, Thermal conductivity in fluorine-doped single-walled carbon nanotubes, Materialia 23 (2022) 101613.
[25] D. Sekyi-Arthur, S.Y. Mensah, N.G. Mensah, K.W. Adu, K.A. Dompreh, R. Edziah, Tunable power factor in fluorine-doped single-walled carbon nanotubes, J. Appl. Phys. 128 (2020) 244301.
[26] D. Sekyi-Arthur, M. Egblewogbe, S.Y. Mensah, N.G. Mensah, K.W. Adu, K.A. Dompreh, R. Edziah, S. Atarah, Giant thermoelectric figure of merit in fluorine-doped single-walled carbon nanotubes, Phys. E 144 (2022) 115292.